

PAPER

[View Article Online](#)
[View Journal](#) | [View Issue](#)Cite this: *J. Mater. Chem. A*, 2020, **8**, 7897

Intrinsic chemical reactivity of solid-electrolyte interphase components in silicon–lithium alloy anode batteries probed by FTIR spectroscopy†

Ryan T. Pekarek,^a Alec Affolter,^{ab} Lauryn L. Baranowski,^a Jaclyn Coyle,^{acde} Tingzheng Hou,^{fg} Eric Sivonxay,^f Brenda A. Smith,^e Rebecca D. McAuliffe,^e Kristin A. Persson,^{fg} Baris Key,^h Christopher Ablett,^d Gabriel M. Veith,^f and Nathan R. Neale^{*a}

In this work we report the solid reaction products from the chemical reaction of aprotic battery electrolyte and three purported components of the Si-based anode SEI: SiO₂ nanoparticles (NPs), lithium silicate (Li_xSiO_y) powders, and Si NPs. We use FTIR and classical molecular dynamics/density functional perturbation theory to assess the solid products remaining with these model materials after exposure to electrolyte. The absence of electrochemical bias provides a view of the chemical speciation resulting from early-stage chemical reactivity during battery assembly as well as under open circuit storage conditions. We believe these species represent the initial stages of SEI growth and predict they likely drive subsequent chemical and electrochemical reactions by controlling molecular interactions at the Si active material interface. We find that nominally equivalent materials react differently even before any electrochemistry is performed (e.g., acidic SiO₂ dissolves whereas alkaline SiO₂ is relatively robust), and derive new understanding of the chemical species that could and could not form stable SEI components in Si-based anodes. These results can be used to inform how to passivate Si anode surfaces and potentially generate an artificially engineered SEI that would be stable and enable next-generation battery anodes.

Received 11th December 2019
Accepted 29th March 2020

DOI: 10.1039/c9ta13535a

rsc.li/materials-a

Introduction

Silicon (Si) is an attractive potential replacement for the graphite active anode material in lithium (Li)-ion batteries since Si offers an order of magnitude greater gravimetric capacity and does not suffer from resource limitations compared with graphite.^{1,2} However, Si-based anodes typically suffer from short cycle and calendar lifetimes that have limited their commercial viability. The degradation processes causing instabilities in Si-based anodes are only recently being uncovered and arise in part from the volumetric expansion/contraction during

lithiation/delithiation.^{1,2} Another important factor is that electrolyte mixtures that have been optimized for graphite anodes, generally a combination of linear or cyclic carbonates (e.g., ethylene carbonate, propylene carbonate, dimethyl carbonate) and a Li salt (e.g., lithium hexafluorophosphate), undergo both chemical and electrochemical reactions at the Si surface owing to the unique chemistry of Si *cf.* graphite. These reactions occur immediately following introduction of electrolyte and during charging and discharging cycles to form a solid-electrolyte interphase (SEI), which is composed of a mixture of both organic (reduced electrolyte) and inorganic (lithium salts, oxides, *etc.*) Si surface components. Understanding the SEI plays a key role both in managing the Li-ion inventory and passivating the Si surface, and understanding the combined chemical and electrochemical reactions leading to its formation are critical to developing strategies for improving Si-based anode performance.

Many techniques have been developed to probe the nature of the electrochemically-generated SEI, with recent progress characterizing the ratio and spatial location of organic and inorganic species *via* neutron reflectivity (NR),³ X-ray photoelectron spectroscopy (XPS),^{4–6} scanning spreading resistance microscopy (SSRM) and time-of-flight secondary ion mass spectrometry (ToF-SIMS),^{7,8} surface- and tip-enhanced Raman

^aChemistry and Nanoscience Center, National Renewable Energy Laboratory, Golden, CO, 80401, USA. E-mail: nathan.neale@nrel.gov^bUniversity of Tennessee, Knoxville, TN 37996, USA^cDepartment of Mechanical Engineering, University of Colorado Boulder, Boulder, Colorado 80309, USA^dSandia National Laboratories, Albuquerque, New Mexico 87123, USA^eOak Ridge National Laboratory, Oak Ridge, TN 37830, USA^fDepartment of Materials Science and Engineering, UC Berkeley, Berkeley, CA 94720, USA^gLawrence Berkeley National Lab, Berkeley, CA 94720, USA^hArgonne National Laboratory, Lemont, IL 60439, USA

† Electronic supplementary information (ESI) available. See DOI: 10.1039/c9ta13535a

spectroscopy (SERS and TERS),^{9,10} and classical molecular dynamics/quantum chemical calculations.¹¹ These studies are coming to a consensus that the initial SEI formation under electrochemical bias involves primarily organic species from electrolyte reduction, which under further cycling becomes thinned at the expense of inorganic phases such as lithium silicates (Li_xSiO_y), lithium oxide (Li_2O), lithium peroxide (Li_2O_2), lithium hydroxide (LiOH), and lithium carbonate (Li_2CO_3).

Whereas the inorganic phases can be chemically identified using these spectroscopic methods, the nature of the organic species is more difficult to discern. Several works have made use of Fourier transform infrared spectroscopy (FTIR) to evaluate the organic SEI as well as electrolyte chemistry due to the many IR-active vibrational modes of both salts as well as carbonate solvent comprising the electrolyte and its decomposition products (*i.e.*, the SEI). The carbonyl ($\text{C}=\text{O}$) stretching frequency in particular is sensitive to its chemical structure including coordination by Li^+ cations and therefore yields information regarding the makeup of organic carbonyl-containing species making up the SEI. For example, Yang *et al.* characterized SEI evolution *via* FTIR on planar Si and a carbon/nano-Si composite electrodes, respectively, as a function of bias.¹² Ex-situ studies of solid material left on the Si-based anode surface have provided extremely valuable pictures of the insoluble species following electrochemical cycling.¹³ Model studies on the reactivity of suspected carbonate-based SEI components with electrolyte have shown the inherent (in)stability of individual species making up the SEI and their decomposition to a range of products including CO_2 , LiF , phosphates, and fluorophosphates.¹⁴ *Operando* measurements have shed light on the early-stage SEI growth as a function of potential, with diethylcarbonate (DEC) reduction to ethoxides occurring at ~ 1.5 V and ethylene carbonate (EC) reduction to poly-EC and lithium ethylene decarbonate (LiEDC) initiating at ~ 0.5 V *vs.* Li/Li^+ .¹⁵

In addition to understanding the species that result from electrochemical reactivity, chemical reactivity is critical knowledge that impacts both the early-stage SEI formation as well as the calendar life stability. The native chemistry at the silicon|electrolyte interface will strongly impact the reactivity with electrolyte that occurs immediately following addition of electrolyte during the battery assembly process. Likewise, chemical species that are unstable in the electrolyte and react spontaneously at ambient temperature will never provide a stable SEI and will result in SEI dissolution and calendar life instability.

In this report, we focus on the chemical reactivity processes to better understand the chemical species that result in beneficial passivation of the Si active material surface and those that should be avoided to ensure long-term stability. We select three different model Si anode materials for our investigation: Si nanoparticles (NPs), SiO_2 NPs, and Li_xSiO_y powders. These model systems represent native chemistries at the silicon active material surface as well as known SEI components following electrochemical cycling. We use FTIR spectroscopy and classical molecular dynamics (MD)/density functional perturbation theory (DFPT) to assess the solid products remaining with the

model materials after electrolyte exposure. We find that nominally equivalent materials react differently even before any electrochemistry is performed (*e.g.*, acidic SiO_2 dissolves whereas alkaline SiO_2 is relatively robust), and that certain molecular species at the Si surface (silyl ethers) are stable whereas others (silyl esters and silicon hydrides) are not. Thus, we derive a new understanding of the chemical species that could and could not form electrolyte-stable SEI components in Si-based anodes – providing useful insights into future SEI engineering strategies.

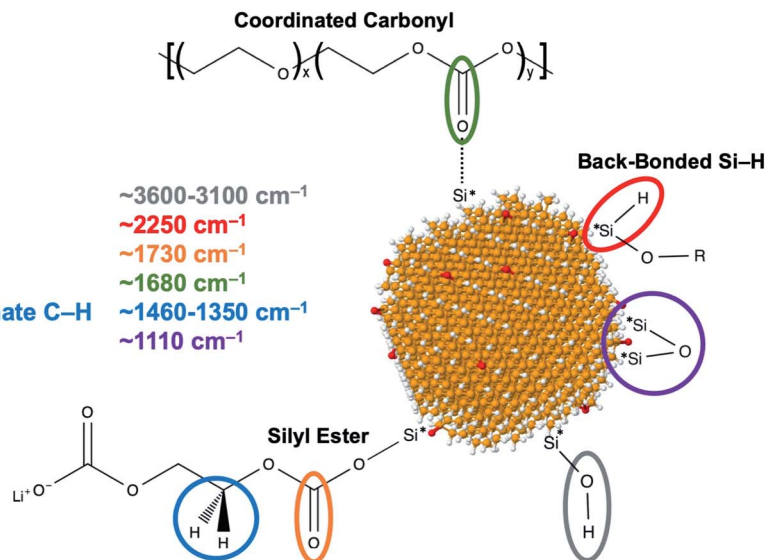
Results and discussion

The results from this study emphasize the importance of fundamental studies to better clarify SEI formation reactions and how these ultimately impact the SEI growth and dissolution both under electrochemical polarization and storage at open circuit. Model Si anode materials are exposed to either 1.2 M LiPF_6 in EC or the so-called Gen2 comprised of 1.2 M LiPF_6 in 3 : 7 (w/w) EC/EMC (EMC = ethyl methyl carbonate) electrolytes at ambient temperature under argon atmosphere for 1–3 days and subsequently washed with a toluene/acetonitrile mixture to remove excess electrolyte. The solid material collected following the washing step is then deposited on a reflective substrate and interrogated *via* diffuse reflectance infrared Fourier transform spectroscopy (DRIFTS, hereafter referred to simply as FTIR). In this way, we can glean information on both the chemical reactivity of the powdered samples with electrolyte as well as the insoluble products from these reactions.

Scheme 1 shows the primary conclusions from this work: (1) different forms of SiO_2 exhibit substantially different chemical reactivity with electrolyte; (2) different phases of lithium silicates Li_xSiO_y , a potential SEI component, react distinctly with electrolyte; (3) silicon hydride $^*\text{SiH}_x$ species on the surface of Si NPs (where $^*\text{Si}$ denotes a surface Si atom) are highly reactive with electrolyte and form a range of electrolyte decomposition reactions; and (4) silyl esters $^*\text{Si}-\text{OC}(\text{O})\text{R}'$ are unstable against electrolyte whereas silyl ethers $^*\text{Si}-\text{OR}$ are much more stable (R , R' = hydrocarbon). In the subsequent sections we present the experiments and data that lead to these conclusions.

The two electrolytes used in this study are 1.2 M LiPF_6 in ethylene carbonate (EC) as well as Gen2 electrolyte. The FTIR spectra of related electrolytes have been characterized in part previously, but we were unable to find complete characterization essential to the present study, particularly for EMC-based electrolytes. Thus, FTIR data and peak assignments for both electrolytes are presented in Fig. 1 and Table 1. The electrolytes exhibit clear evidence of substantial coordination of carbonate solvent to the Li^+ cation *via* conventional solvent-separated ion pair (SSIP) $[\text{Li}^+(\text{EC})_{6-x}(\text{EMC})_x]\text{PF}_6^-$ as well as contact ion pair (CIP) $[\text{Li}^+(\text{EC})_{5-x}(\text{EMC})_x\text{PF}_6^-]$ structures (see Fig. S1†).^{16–18}

For the carbonate modes, FTIR data do not distinguish between SSIP and CIP coordination, only between carbonates coordinated to Li^+ and uncoordinated carbonates not bound to Li^+ (*i.e.*, coordinated carbonates form the first solvent shell around Li^+ and uncoordinated carbonates are the “free” solvent; see Fig. S1†). For the 1.2 M LiPF_6 electrolyte (blue spectrum,



Scheme 1 Summary of surface functionalities identified *via* FTIR spectroscopy from reaction between Si NPs, SiO₂ NPs, or Li_xSiO_y powders and LiPF₆ carbonate electrolytes in this work. In the Si NP cartoon, Si = orange, H = white, and O = red.

Fig. 1), our data are consistent with previously assigned uncoordinated (uc) and coordinated (c) EC carbonyl stretching ($\nu_{\text{C=O}}$) modes at 1797 and 1763 cm^{-1} , respectively. Similar differences between c and uc EC populations are apparent in the $\nu, \delta_{\text{C-H}}$ modes from 1371–1481 cm^{-1} , the $\nu_{\text{C-O}}$ modes from 1069–1306 cm^{-1} , and the $\delta_{\text{C-H}}$ and $\delta_{\text{C=O}}$ EC ring modes from 716–775 cm^{-1} . From the intensity of c and uc peaks at this 1.2 M LiPF₆ concentration, it appears that substantially more EC is the c *versus* uc state. The Gen2 FTIR spectrum is significantly more complex, with modes from both EC and EMC apparent in these same spectral regions (red spectrum, Fig. 1). Whereas the $\nu_{\text{C=O}}$ EC modes shift to slightly higher energies relative to those in

1.2 M LiPF₆ in EC electrolyte, the other EC modes are unchanged, suggesting the strongest solvent effects occur on the $\nu_{\text{C=O}}$ frequency as would be expected from Li-ion coordination *via* this functional group.

Making quantitative assessment from these EC carbonyl uc/c ratios from the $\nu_{\text{C=O}}$ region is complicated by overlapping EC ring overtone modes,^{19–21} and similar complications exist in most other parts of the spectra. However, Henderson and coworkers have proposed that the integral area of the $\delta_{\text{C=O}}$ EC ring bending modes (observed here at 728 and 716 cm^{-1} for c and uc, respectively) can be used to quantify the ratio, provided the integrated peak areas are further scaled by a factor

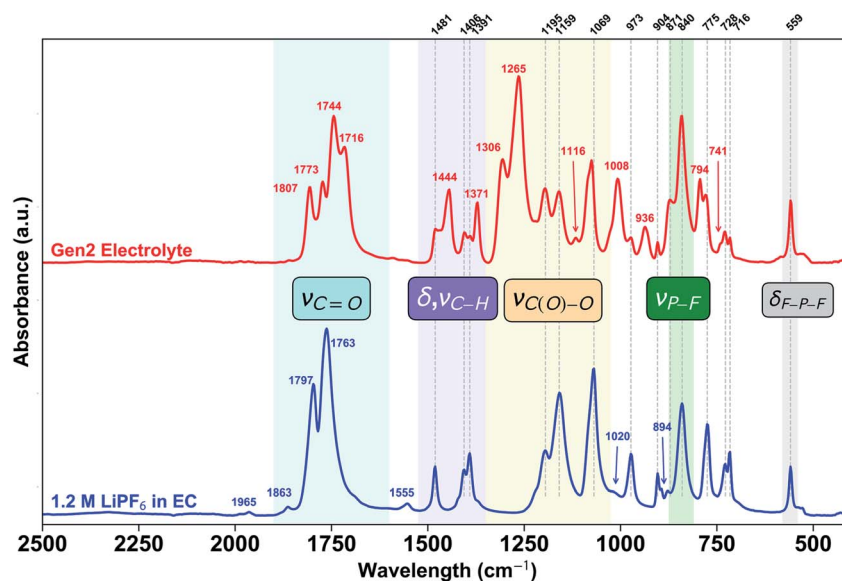


Fig. 1 ATR-FTIR spectra of 1.2 M LiPF₆ in EC (blue) and Gen 2 (red) electrolytes. Peak positions in blue are unique to 1.2 M LiPF₆ in EC, those in red are unique to Gen 2, and those in black marked with dashed gray lines are common to both spectra. Assignments for all peaks are given in Table 1.

Table 1 Infrared frequency band assignments for 1.2 M LiPF₆ in EC and Gen 2 electrolytes. Carbonate complexation of the Li⁺ cation from both conventional tetra-coordination of the Li cation *via* four carbonate solvent molecules [Li⁺(EC)_{4-x}(EMC)_xPF₆⁻] as well as contribution from the contact ion pair [Li⁺(EC)_{3-x}(EMC)_xPF₆⁻] are evident in the spectra. Some assignments in this work were made by comparison to the FTIR spectra of dimethylcarbonate (DMC)²³ and methyl *tert*-butyl ether (MTBE).²⁴ s = strong; m = medium; w = weak; v = very; sh = shoulder

Observed Frequency (cm ⁻¹)	Assignment	Source
1965 (vw)	EC combination of 1069 cm ⁻¹ + 894 cm ⁻¹	25
1863 (vw)	Not assigned	
1807 (m)	ν C=O, EMC-EC, uncoordinated (uc)	This work
1797 (s)	ν C=O, EC, uc and overtone of 893 cm ⁻¹	18, 25 and 26
1773 (m)	ν_s C=O, EMC-EC, coordinated (c)	This work
1763 (vs)	ν_s C=O, EC, c	18 and 26
1744 (s)	ν_s C=O, EMC-EC, uc	This work
1716 (m)	ν_s C=O, EMC-EC, c	This work
1555 (vw)	EC overtone of 775 cm ⁻¹	25
1481 (w)	δ_s CH ₂ scissor, EC, uc	25 and 26
1444 (m)	ν_a CH ₃ deformation, EMC (OCH ₂ CH ₃ & OCH ₃), uc	This work
1406 (w)	δ_s CH ₂ wag, EC, c	26
1391 (m)	δ_s CH ₂ wag, EC, uc	25 and 26
1371 (m)	ν_s CH ₃ deformation, EMC (CH ₂ CH ₃), uc	This work
1306 (m)	ν C(O)-O, EMC, c	This work
1265 (m)	ν C(O)-O, EMC, uc	This work
1195 (m)	ν_a C(O)-O, ring EC, c	26
1159 (s)	ν_a C(O)-O, ring EC, uc	25 and 26
1116 (vw)	ν_s C-O, ring EC, c	This work
1069 (s)	ν_s C-O, ring EC and EMC, uc	25 and 26
1020 (vw, sh)	Not assigned	
1008 (m)	Not assigned	
973 (m)	ν_s skeletal stretching, ring EC, uc	25 and 26
936 (w)	Not assigned	
904 (w)	EC ring breathing symmetric mode	19
894 (vw)	ν_s skeletal breathing, ring EC, uc	25
871 (w)	ν_s P-F, PF ₆ ⁻ , c <i>via</i> contact ion pair	17 and 27
840 (s)	ν_s P-F, PF ₆ ⁻ , uc	17 and 27
794 (m)	Not assigned	
775 (m)	ρ_a CH ₂ rocking in-phase, EC, uc	25
741 (vw, sh)	Not assigned	
728 (w)	δ_s C=O bending in-plane, EC, c	19
716 (m)	δ_s C=O bending in-plane, EC, uc	19 and 25
559 (w)	δ_s F-P-F bending, PF ₆ ⁻ , uncoordinated	28

determined by DFPT calculations to determine the population (because c and uc states have different IR absorption oscillator strengths).²² Applying this scaling factor to our data, we find that the EC uc/c ratio changes from 0.64 in 1.2 M LiPF₆/EC to 0.47 in Gen2 electrolyte. Thus, the presence of EMC in the Gen2 electrolyte drives far more EC into the coordinated state despite EC's far lower concentration (30 wt%; *cf.* 70 wt% for EMC) in the Gen2 electrolyte.

Two major conclusions can be drawn from these data. First, EC appears to outcompete EMC for Li-ion coordination, with the EC uc/c ratio of 0.47 and that for EMC 0.72 in Gen2 electrolyte. Otherwise, if the Li-ion binding affinities for EMC and EC were similar, we would expect similar uc/c ratios of \sim 0.64 (the uc/c ratio in 1.2 M LiPF₆ in EC) for each carbonate in both electrolytes. This result concurs with the established preference for Li-ion coordination by cyclic EC *versus* linear dimethyl carbonate (DMC) from gas-phase chemistry and QC and *ab initio* MD simulations.²² A second major conclusion can be drawn by close inspection of the ν_{P-F} modes at 840 and 871 cm⁻¹, where the former represents the P-F stretch

associated with PF₆⁻ in the SSIP and the latter higher energy stretching frequency with that of the CIP. Based on the spectra in Fig. 1, we find that it is possible to resolve the relative SSIP/CIP ratios in these two electrolytes. For the 1.2 M LiPF₆ electrolyte, an intense peak at 840 cm⁻¹ from the ν_{P-F} stretching mode for the SSIP dwarfs that of the CIP at 871 cm⁻¹ (blue spectrum, Fig. 1). In contrast, the presence of EMC in the Gen2 electrolyte results in a much greater amount of the ν_{P-F} stretching mode for the CIP (red spectrum, Fig. 1). This result clearly shows that Gen2 contains more CIPs than 1.2 M LiPF₆ in pure EC electrolyte, which is dominated by the nearly exclusive SSIP structure around the Li-ions consistent with our recent report showing an 88/12 SSIP/CIP ratio in 1.2 M LiPF₆ in EC.¹¹ Since more CIPs reduce the total Li-ion coordination number, this result also means that the above calculation of the EMC uc/c ratio of 0.72 is an overestimation of the ability of EMC to coordinate Li-ions, and the actual EMC uc/c ratio is likely greater (*i.e.*, less c EMC in Gen2 electrolyte).

The experimental results are further compared with theoretical calculation results where two electrolyte systems—1.2 M

LiPF₆ in EC and the Gen2 electrolyte—were simulated using classical MD. The Gen2 electrolyte exhibits a much higher degree of CIP (more than 30%) formation as compared to 1.2 M LiPF₆ in EC electrolyte (12%), which is consistent with the FTIR results.

Silica

FTIR spectra of samples before and after electrolyte exposure for three different forms of silica (SiO₂) are shown in Fig. 2: fumed SiO₂ (0.2–0.3 μm, Sigma-Aldrich, S5505), NanoAmor (Nano-structured & Amorphous Materials, Inc.) Silicon, and Stöber SiO₂. Fumed SiO₂ is a commercial product prepared by flame pyrolysis of SiCl₄ in dry oxygen or air and thus gives a highly acidic form of SiO₂. NanoAmor Silicon (30–50 nm; Stock# 0141JS) is a commercial product prepared by milling silicon and frequently has been used in battery research. We group this 30–50 nm NanoAmor Silicon with the SiO₂ reactivity since our characterization of this material *via* solid-state ²⁹Si NMR spectroscopy shows that it is comprised primarily (~80%) of SiO₂ (Fig. S3†). Stöber SiO₂ is prepared through a sol-gel process of controlled hydrolysis of tetraethylorthosilicate that gives a more basic surface²⁹ than fumed SiO₂.

As shown in the blank spectra of as-received samples in Fig. 2, before reaction with electrolyte, all three samples exhibit broad absorption in the $\nu_{\text{Si-O-Si}}$ stretching region from *ca.* 1060–1210 cm⁻¹ prior to reaction with electrolyte. This broad feature is characteristic of oxidized silicon and is derived from a complex surface structure resulting from geminal hydroxyl groups (Q₂), free silanol groups (Q₃), H-bonded silanol groups (Q₃'), and siloxane groups (Q₄) as characterize in our prior work.³⁰

Upon exposure to electrolyte and washing, the three different SiO₂ samples react with electrolyte to give solid products in unique ways. First, we observe that a transparent, colorless solution is formed by soaking fumed SiO₂ in Gen2 electrolyte for 24 h, suggesting that this highly acidic form of SiO₂ completely dissolves. Following addition of non-polar toluene and subsequent washing, a colorless solid precipitates that is comprised largely of intense peaks centered at 1265 and 1167 cm⁻¹ with no prominent $\nu_{\text{Si-O-Si}}$ stretching mode. Bellamy previously has assigned vibrations from CH₃Si-O and RSi-O_{1.5} at 1260 and 1160 cm⁻¹, respectively,³¹ and it is plausible that these species form a large part of the precipitated materials following reaction and precipitation. In addition, we observe an intense, broad new feature at ~730 cm⁻¹ (red spectrum, Fig. 2a) and weak intensity peaks in the carbonyl (1816, 1788, and 1755 cm⁻¹) and C-H bending (1481–1377 cm⁻¹) regions. These data suggest that the solid precipitated from the dissolved fumed SiO₂/Gen2 reaction does not contain appreciable amounts of carbonate byproducts. Regardless of the actual chemical makeup of the precipitated product, this experiment shows that acidic SiO₂ is chemically unstable to Gen2 electrolyte.

Next, the as-received 30–50 nm NanoAmor particles exhibit the expected broad $\nu_{\text{Si-O-Si}}$ stretch from *ca.* 1060–1210 cm⁻¹ as well as distinct $\nu_{\text{Si-H}}$ modes characteristic of surface hydrides

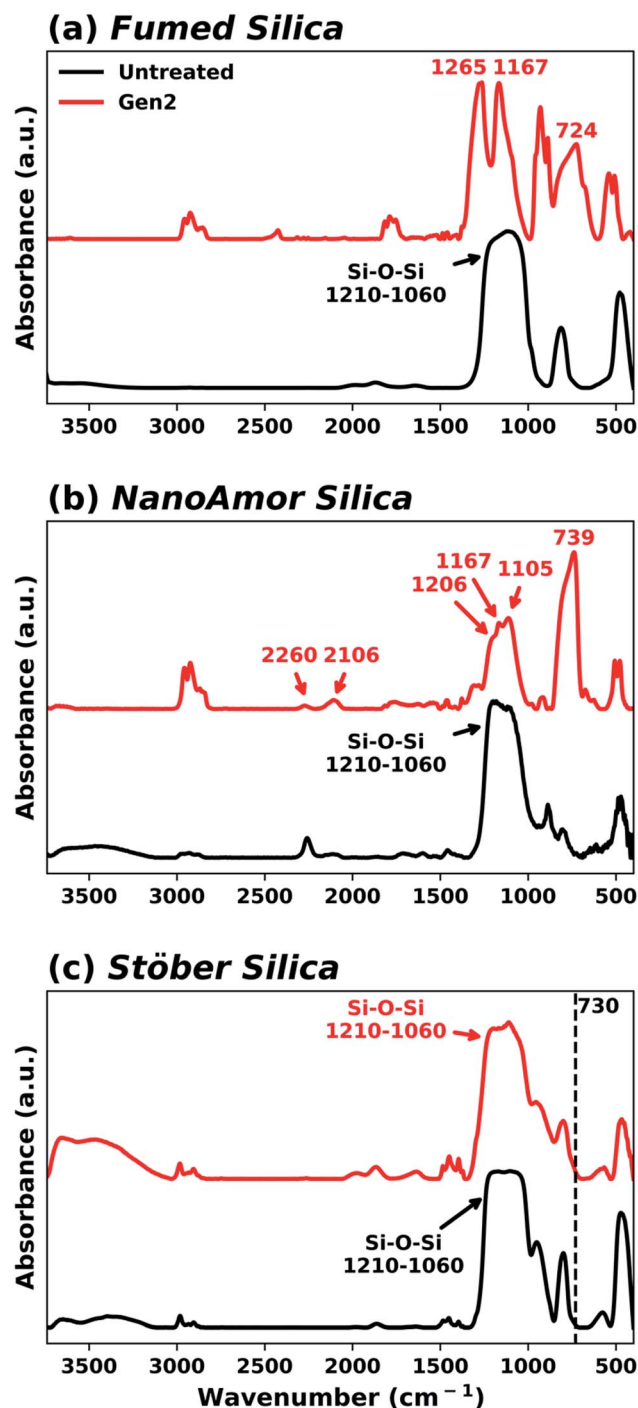


Fig. 2 FTIR spectra showing (a) Fumed SiO₂, (b) NanoAmor 30–50 nm Silicon, and (c) Stöber SiO₂ before (black) and after (red) exposure to Gen2 electrolyte.

from both clean (*i.e.*, unoxidized) *SiH_x at 2106 cm⁻¹ as well as so-called “back-bonded” (O_y)*SiH_x at ~2260 cm⁻¹ (black spectrum, Fig. 2b),^{32,33} which is a surface silicon hydride *Si-H where the surface silicon atom *Si also is bound to one or more oxygen groups (see Fig. S4† for a detailed view of the $\nu_{\text{Si-H}}$ region and chemical structures for the back-bonded (O_y)*SiH_x). Following reaction with electrolyte, the $\nu_{\text{Si-H}}$ region changes substantially, with an increase in intensity of clean *SiH_x

relative to oxidized $(\text{O}_y)^*\text{SiH}_x$ (red spectrum, Fig. 2b). The $\nu_{\text{Si-O-Si}}$ stretching region also decreases in intensity, and an intense, broad new feature appears near 730 cm^{-1} . As with fumed SiO_2 , these data suggest that the SiO_2 on the NanoAmor particles dissolves in Gen2 electrolyte that ultimately gives rise to an insoluble species following the washing procedure with an intense IR signature at $\sim 730\text{ cm}^{-1}$. The dissolution of silica surfaces is consistent with what has been reported previously in the literature using reflectometry.³⁴

Surprisingly, Stöber SiO_2 particles with more basic surface chemistries (*cf.* fumed SiO_2) display relatively low reactivity with Gen2 electrolyte. As shown in Fig. 2c, the $\nu_{\text{Si-O-Si}}$ stretching region in Stöber SiO_2 is minimally perturbed following exposure to electrolyte. Similarly, no feature at $\sim 730\text{ cm}^{-1}$ resulting from SiO_2 dissolution and precipitation is observed. These data are clear that acidic SiO_2 is highly reactive toward Gen2 electrolyte, while more basic SiO_2 is relatively stable toward electrolyte. Given the presence of acid (HF) in PF_6 -containing electrolytes and the fact that the vast majority of Si NPs used in Si-based anodes are heavily oxidized, the presence of SiO_2 likely is a significant source of SEI instability.

Lithium silicates

Similar to SiO_2 , lithium silicates of the molecular formula Li_xSiO_y also are purported components of the SEI.⁵ Our prior theoretical work detailed the ternary phase diagram comprising Li, Si, and O as well as the bulk moduli and electrochemical behavior of Li_xSiO_y ,⁵ and our prior experiments on amorphous thin film $\text{Li}_2\text{Si}_2\text{O}_5$ showed significant chemical and electrochemical reactivity in Gen2 electrolyte after just 3 h.^{35,36} Here we probe the chemical reactivity of crystalline lithium silicate powders of the Li_2SiO_3 and Li_4SiO_4 phases with Gen2 electrolyte and find that the crystalline Li_2SiO_3 phase shows significant reactivity – similar to the amorphous material – whereas the crystalline Li_4SiO_4 phase exhibits relatively less chemical reactivity toward electrolyte (*cf.* Li_2SiO_3 or amorphous Li_4SiO_4). As can be seen in Fig. 3, lithium silicate FTIR spectra display many unique features distinct from SiO_2 . Whereas the SiO_2 spectra contain few stretches above 1400 cm^{-1} , both lithium silicate samples show stretches $1850\text{--}2100\text{ cm}^{-1}$ and $1300\text{--}1400\text{ cm}^{-1}$ that are likely a result of carbonate impurities within the particles resulting from their synthesis.³⁷ Following exposure to Gen2 electrolyte, the Li_2SiO_3 sample appears to coordinate either EC or EMC from the electrolyte as evidenced by key new features at 1814 and 1781 cm^{-1} (comparable to the *uc/c* carbonyl stretching frequencies at $1807/1773\text{ cm}^{-1}$ in free Gen2 electrolyte) and prominent C(O)–O stretching modes at 1300 and 1210 cm^{-1} (close to EMC and ring EC coordination modes at 1306 and 1195 cm^{-1} , respectively, in free Gen2 electrolyte; see Fig. 1 and Table 1). While this reactivity doesn't appear to substantially change the Li_2SiO_3 bulk, it does suggest that this material interacts strongly with carbonates. In contrast, very minimal differences between the Li_4SiO_4 sample before and after Gen2 electrolyte exposure are observed, suggesting that with this Li_xSiO_y phase neither the bulk or surface are reactive toward electrolyte.

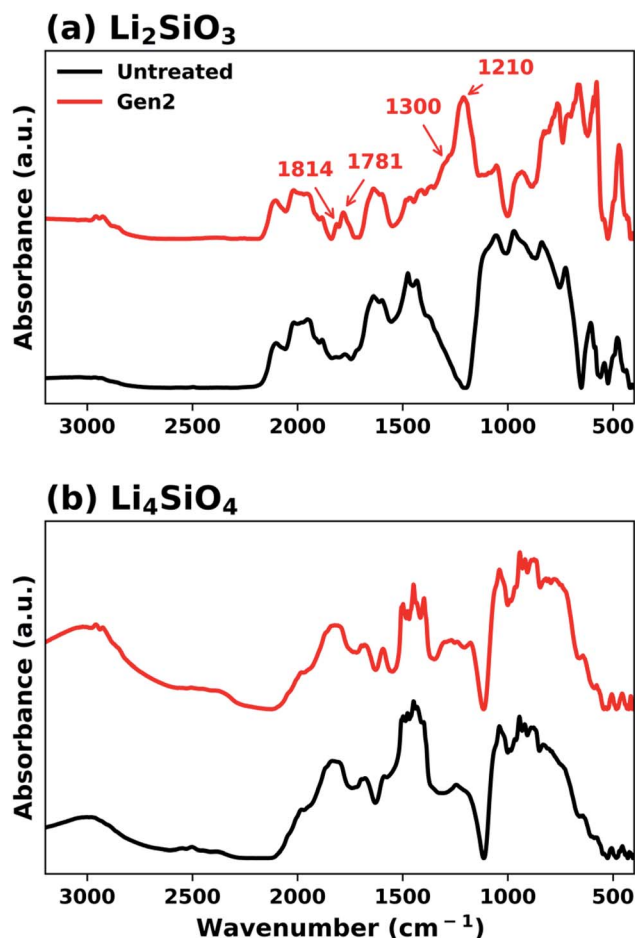


Fig. 3 DRIFTS spectra showing Li_2SiO_3 (a) and Li_4SiO_4 (b) before (black) and after (red) exposure to Gen2 electrolyte.

The lack of bulk reactivity between lithium silicates and electrolyte observed *via* FTIR are corroborated by neutron pair distribution function (nPDF) experiments. Here, three different silicate powders, Li_2SiO_3 , $\text{Li}_2\text{Si}_2\text{O}_5$ and Li_4SiO_4 , were first loaded in a glove box and subjected to a $500\text{ }^\circ\text{C}$ anneal for 2 h to remove water and any residual surface carbonates from synthesis. Next, the materials were soaked in Gen2 electrolyte at $60\text{ }^\circ\text{C}$ for 3 days, and washed with dimethylcarbonate (DMC, 15 mL aliquots) four times and drying under vacuum prior to loading into glass capillaries for nPDF data collection. In Fig. S5,[†] the black lines are the data collected for the pristine samples while the red dashed line shows the data after electrolyte exposure. From this data there is no evidence of changes to the bulk structure of the Li–Si–O materials. Furthermore, there is no evidence of the formation of an amorphous surface phase, on the crystalline materials, which would have manifested as new peaks and valleys in the data. Finally we find no evidence for significant concentrations of organic species in or on the sample, which would attenuate the neutron signal due the absorption of neutrons by H.

Together this indicates that crystalline Li–Si–O are very stable against the electrolyte. This is true at high temperatures where one would expect greater reactivity. Furthermore, we see

no evidence of other significant lithium or organic phases trapped on the surface. This data does not exclude catalytic activity of the materials but does point to stability in the crystalline phase. This is in contrast to the data measured for amorphous materials reported previously which demonstrated significant electrolyte reactivity.

Silicon hydrides, esters, and ethers

Si NPs grown from the gas-phase decomposition of silane (SiH_4) using the nonthermal plasma method³⁸ exhibit clean, virtually oxide-free surfaces comprised of silicon hydrides $^*\text{SiH}_x$ where $x = 1, 2$, or 3 . Our previous works have mapped out the FTIR signatures,³⁹ ^1H and ^{29}Si NMR shifts,^{33,40} radical-initiated surface reactivity for these NPs,⁴¹ as well as up to 97.9% capacity retention in half-cell configuration with water-processed Si NPs surface functionalized with oligo(ethylene oxide)-epoxy ligands.⁴² DRIFTS spectra of as-prepared SiH_x -terminated Si NPs exhibit a broad peak corresponding to the $\nu_{\text{Si-H}}$ stretching region ($2000\text{--}2300\text{ cm}^{-1}$), with peaks at 2138 , 2110 , and 2087 cm^{-1} characteristic of the $^*\text{SiH}_3$, $^*\text{SiH}_2$, and $^*\text{SiH}$ surface terminations,³⁹ as well as Si-H scissor (910 , 863 cm^{-1}) and wag (669 cm^{-1}) modes; additional longitudinal acoustic phonon modes ω_{TO} are evident at 490 cm^{-1} .⁴³ (Fig. 4, black spectrum). As such, these plasma-grown Si NPs provide a unique platform to study the chemical reactivity of silicon surfaces with Li-ion carbonate electrolytes. First, we note that these SiH_x -terminated Si NPs (hereafter referred to simply as SiH_x -Si NPs) are highly oxophilic and react spontaneously with oxygen sources at ambient temperature. For example, the slow development of SiO_2 occurs over a period of weeks occurs when as-grown SiH_x -Si NPs are stored in an argon-filled glove box *via* reaction with trace $\text{H}_2\text{O}/\text{O}_2$ impurities (Fig. S6†).

Given this extreme reactivity to trace O-containing species, it comes as no surprise that these SiH_x -Si NPs are extremely reactive toward Li-ion carbonate electrolytes. Indeed, the FTIR spectra of SiH_x -Si NPs following exposure to Gen2 electrolyte exhibit a multitude of new peaks corresponding to a range of Si-

O species resulting from the this reactive surface and oxophilic nature of Si. As shown in Fig. 4 (red spectrum), the $\nu_{\text{Si-H}}$ stretching region features a new shoulder at 2244 cm^{-1} assigned to a “back-bonded” $(\text{O}_y)^*\text{SiH}_x$ (the same functionality described for the NanoAmor Si NPs, Fig. 2 and S4†).

Further insight into the nature of the surface is found in the $\nu_{\text{C=O}}$ region, which shows low energy peaks at 1730 and 1681 cm^{-1} not present in the Gen 2 electrolyte. We assign the feature at 1730 cm^{-1} to a $^*\text{Si-OC(O)R'}$ ester^{13,44} and that at 1681 cm^{-1} —which is too low energy for an anhydride, ester, ketone, or aldehyde—to carbonyl coordination to $^*\text{Si}$. For example, the $\nu_{\text{C=O}}$ in 2-butanone is known to shift from 1712 cm^{-1} to 1687 cm^{-1} as well as give rise to an even lower energy carbonyl feature at 1610 cm^{-1} upon coordination to a surface $^*\text{Si}$ atom *via* a hypervalent interaction (*i.e.*, a 5-coordinate Si*) in H,Cl-terminated Si NCs.⁴⁵ To verify the assignment of the peak, DFPT calculations were performed to obtain the theoretical FTIR spectra of Si surface adsorbed EC molecules (Fig. S7†). The model was built with a (111) Si slab and a EC molecule added above the slab with the C=O bond perpendicular to the slab surface. The spectra clearly shows a $\nu_{\text{C=O}}$ peak for an EC coordinated to a $^*\text{Si}$ surface at a frequency of 1695 cm^{-1} , which indicates that the low energy peak at 1681 cm^{-1} originates from the carbonyl coordination to $^*\text{Si}$.

Similar to the carbonyl region, other regions of the FTIR spectrum show several new features. The C-H bending region exhibits two new intense peaks at 1457 and 1375 cm^{-1} likely resulting from ring-opening of EC⁴⁶ and/or reaction with EMC *via* radical-based processes to give either alkoxy- or carboxylate-functionalized Si NCs. Smaller but still evident C(O)-O vibrations at 1294 , 1257 , 1239 , and 1147 cm^{-1} at the high energy side of the very broad $\nu_{\text{Si-O-Si}}$ feature centered at 1110 cm^{-1} demonstrate the complex nature of the surface species present following reaction of Gen2 with $^*\text{SiH}_x$ -Si NCs (see Fig. S8†). As-prepared $^*\text{SiH}_x$ -Si NCs are additionally treated with 1.2 M LiPF_6 in EC to compare its reactivity relative to Gen2. After this

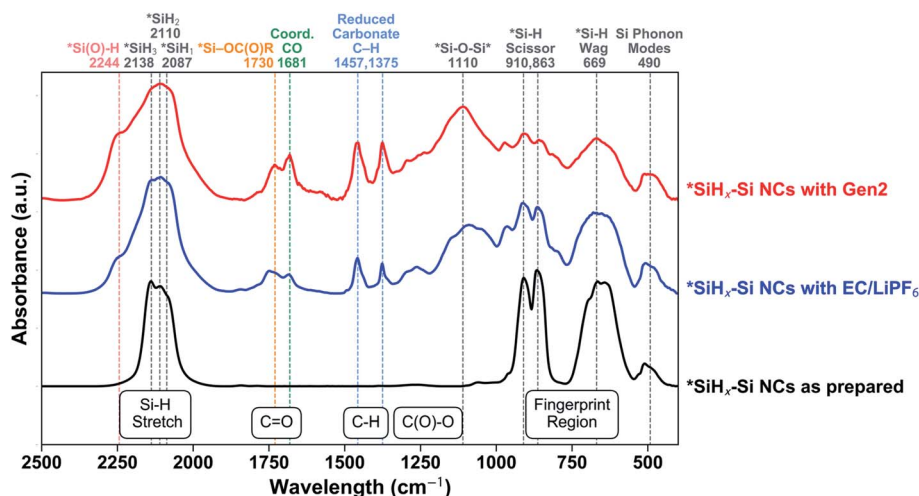


Fig. 4 Normalized FTIR spectra of $^*\text{SiH}_x$ -Si NCs before (black) and after exposure to 1.2 M LiPF_6 in EC (blue) and Gen 2 (red) electrolytes.

reaction, we observe similar $\nu_{\text{C=O}}$ modes from $^*\text{Si-OC(O)R}$ ester and $^*\text{Si-carbonyl}$ coordination (1749 and 1681 cm^{-1} , respectively), C-H bends (1457 and 1375 cm^{-1}), C(O)-O and/or $\text{R}^*\text{Si-O}$ stretches (1294 , 1263 and 1147 cm^{-1}), and the $\nu_{\text{Si-O-Si}}$ mode (1092 cm^{-1} ; Fig. 4, blue spectrum). In summary, it is clear that these hydride-terminated $^*\text{SiH}_x\text{-Si}$ NPs react strongly with carbonate electrolytes to generate a number of surface species corresponding to electrolyte reduction and oxidation that forms the initial SEI prior to polarization-induced SEI growth.

Based on these results, we chose to intentionally modify the surface of plasma-synthesized Si NPs with ester ($^*\text{Si-OC(O)R'}$) or ether ($^*\text{Si-OR}$) functionalities and subject these functionalized Si NPs to either 1.2 M LiPF_6 in EC or Gen2 electrolytes using the same ambient temperature soaking conditions. In this way, we could explore the chemical (in)stability of silyl ester and ether functionalities to electrolyte. As-grown, hydride-terminated $^*\text{SiH}_x\text{-Si}$ NPs are functionalized with benzoyl carboxylate (forming a silyl ester $^*\text{Si-OC(O)R'}$ where R' = phenyl, Ph) and *tert*-butoxide (forming a silyl ether $^*\text{Si-OR}$ where R = *tert*-butyl, ^tBuO) *via* organic peroxide-based chemistry (see Experimental section for full details). Fig. 5 shows the critical $\nu_{\text{Si-H}}$ stretching region of these functionalized Si NPs before and after exposure to electrolyte. From these data it is clear that electrolyte causes the “back-bonded” $(\text{O}_y)^*\text{SiH}_x$ to disappear entirely from the silyl ester Ph(O)CO-Si NPs, whereas this species is retained for

$^t\text{BuO-Si}$ NCs. This result shows that silyl ether groups $^*\text{Si-OC(O)R'}$ are unstable chemically against electrolyte, and that silyl ether $^*\text{Si-OR}$ groups are relatively chemically stable. This important conclusion means that chemical or electrochemical formation of silyl esters $^*\text{Si-OC(O)R'}$ is highly undesirable and will never lead to a stable SEI. This does not mean that Si NPs functionalized with silyl ether $^*\text{Si-OR}$ groups are a panacea providing a stable SEI, as additional complex reactivity with electrolyte is observed in the full spectral data (Fig. S9†), presumably *via* reaction between residual surface hydrides $^*\text{SiH}_x$ and electrolyte. Still, these results provide a window into the species that should and should not be incorporated into an artificially-engineered SEI.

Conclusions

In this report we detail the solid products resulting from chemical reactions between Li-based carbonate electrolytes and SiO_2 , Li_xSiO_y , and Si materials. The absence of electrochemical bias provides a view of the chemical speciation resulting from early-stage SEI growth during the first stages of battery assembly as well as under open circuit storage conditions. First, we provide comprehensive characterization of both 1.2 M LiPF_6 in EC as well as 1.2 M LiPF_6 in 30/70 (w/w) EC/EMC (*i.e.*, Gen2) electrolytes. Second, we identify a number of key conclusions based on the chemical reactivity studies *via* FTIR spectroscopy and DFPT calculations. We find that acidic SiO_2 is highly reactive toward electrolyte, whereas alkaline SiO_2 is more chemically stable. We additionally show that amorphous Li_2SiO_3 coordinates carbonate *via* a physisorbed interaction, whereas amorphous Li_4SiO_4 is comparably unreactive. Finally, we find that hydride-terminated Si nanoparticles are highly reactive with electrolyte, and that silyl ether surface functionalities are relatively robust whereas silyl esters are not. Ultimately, these results can be used to inform how to passivate Si anode surfaces and potentially generate an artificially engineered SEI that would be stable and enable next-generation battery anodes.

Conflicts of interest

There are no conflicts to declare.

Acknowledgements

This research was supported by the U.S. Department of Energy's Vehicle Technologies Office under the Silicon Electrolyte Interface Stabilization (SEISta) Consortium directed by Brian Cunningham and managed by Anthony Burrell. This work was conducted in part by the Alliance for Sustainable Energy, LLC, the manager and operator of the National Renewable Energy Laboratory for the U.S. Department of Energy (DOE) under Contract No. DE-AC36-08GO28308, and the Oak Ridge National Laboratory, managed by UT Battelle, LLC, for the U.S. Department of Energy (DOE) under contract DE-AC05-00OR22725. A portion of this research, used resources at the Spallation Neutron Source, nPDF – NOMAD Beamline, a DOE Office of Science User Facility operated by the Oak Ridge National

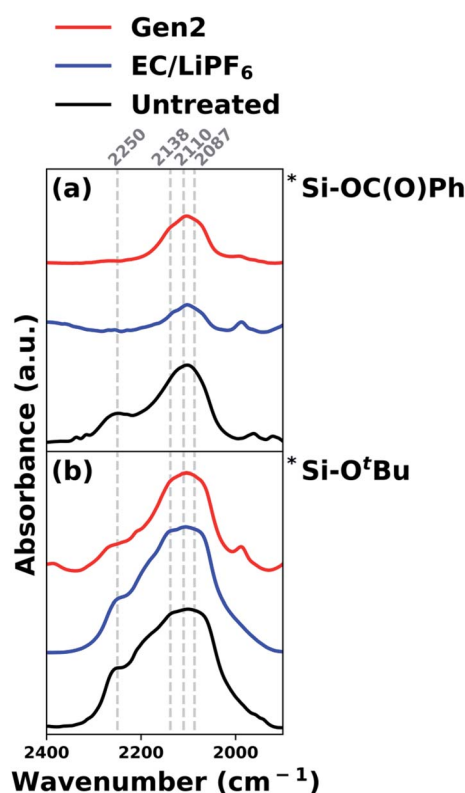


Fig. 5 FTIR spectra showing reaction of 1.2 M LiPF_6 in EC (blue) and Gen 2 (red) electrolytes with Ph(O)CO-Si (a) and $^t\text{BuO-Si}$ (b) and NCs. The “back-bonded” $(\text{O}_y)^*\text{SiH}_x$, $^*\text{SiH}_3$, $^*\text{SiH}_2$ and $^*\text{SiH}$ stretches are marked by the dashed gray lines at 2250 , 2138 , 2110 and 2087 cm^{-1} , respectively.

Laboratory. Sandia National Laboratories is a multimission Laboratory managed and operated by National Technology & Engineering Solutions of Sandia, LLC, a wholly owned subsidiary of Honeywell International Inc., for the U.S. Department of Energy's National Nuclear Security Administration under contract DE-NA0003525. Solid-state NMR conducted at Argonne National Laboratory was supported by the U.S. Department of Energy, Office of Vehicle Technologies, under Contract No. DE-AC02-06CH11357. Argonne, a U.S. Department of Energy Office of Science laboratory, is operated under Contract No. DE-AC02-06CH11357. Additionally, a portion of the modeling work was funded by the Battery Materials Research (BMR) program, under the Assistant Secretary for Energy Efficiency and Renewable Energy, Office of Vehicle Technologies of the U.S. Department of Energy, Contract No. DE-AC02-05CH11231. Computational simulations presented in this article utilized resources of the National Energy Research Scientific Computing Center, a U.S. Department of Energy Office of Science User Facility operated under Contract No. DE-AC02-05CH11231. The views expressed in the article do not necessarily represent the views of the DOE or the U.S. Government. The U.S. Government retains and the publisher, by accepting the article for publication, acknowledges that the U.S. Government retains a nonexclusive, paid-up, irrevocable, worldwide license to publish or reproduce the published form of this work, or allow others to do so, for U.S. Government purposes. Images used in the table of contents graphic were used with permission from Timothy Meinburg and Jeremy Bishop on Unsplash.

References

- 1 M. N. Obrovac and V. L. Chevrier, *Chem. Rev.*, 2014, **114**, 11444–11502.
- 2 D. Ma, Z. Cao and A. Hu, *Nano-Micro Lett.*, 2014, **6**, 347–358.
- 3 G. M. Veith, M. Doucet, R. L. Sacci, B. Vacaliuc, J. K. Baldwin and J. F. Browning, *Sci. Rep.*, 2017, **7**, 6326.
- 4 K. N. Wood and G. Teeter, *ACS Appl. Energy Mater.*, 2018, **1**, 4493–4504.
- 5 Y. Xu, C. Stetson, K. Wood, E. Sivonxay, C. Jiang, G. Teeter, S. Pylypenko, S.-D. Han, K. A. Persson, A. Burrell and A. Zakutayev, *ACS Appl. Mater. Interfaces*, 2018, **10**, 38558–38564.
- 6 Y. Xu, K. Wood, J. Coyle, C. Engtrakul, G. Teeter, C. Stoldt, A. Burrell and A. Zakutayev, *J. Phys. Chem. C*, 2019, **123**, 13219–13224.
- 7 C. Stetson, T. Yoon, J. Coyle, W. Nemeth, M. Young, A. Norman, S. Pylypenko, C. Ban, C.-S. Jiang, M. Al-Jassim and A. Burrell, *Nano Energy*, 2019, **55**, 477–485.
- 8 C. Stetson, Y. Yin, C.-S. Jiang, S. C. DeCaluwe, M. Al-Jassim, N. R. Neale, C. Ban and A. Burrell, *ACS Energy Lett.*, 2019, 2770–2775, DOI: 10.1021/acsenergylett.9b02082.
- 9 G. Yang, R. L. Sacci, I. N. Ivanov, R. E. Ruther, K. A. Hays, Y. Zhang, P.-F. Cao, G. M. Veith, N. J. Dudney, T. Saito, D. T. Hallinan and J. Nanda, *J. Electrochem. Soc.*, 2019, **166**, A178–A187.
- 10 J. Nanda, G. Yang, T. Hou, D. N. Voylov, X. Li, R. E. Ruther, M. Naguib, K. Persson, G. M. Veith and A. P. Sokolov, *Joule*, 2019, **3**, 2001–2019.
- 11 T. Hou, G. Yang, N. N. Rajput, J. Self, S.-W. Park, J. Nanda and K. A. Persson, *Nano Energy*, 2019, **64**, 103881.
- 12 J. Yang, N. Solomatin, A. Kraysberg and Y. Ein-Eli, *ChemistrySelect*, 2016, **1**, 572–576.
- 13 C. C. Nguyen, T. Yoon, D. M. Seo, P. Guduru and B. L. Lucht, *ACS Appl. Mater. Interfaces*, 2016, **8**, 12211–12220.
- 14 B. S. Parimalam, A. D. MacIntosh, R. Kadam and B. L. Lucht, *J. Phys. Chem. C*, 2017, **121**, 22733–22738.
- 15 Y. Horowitz, H.-L. Han, P. N. Ross and G. A. Somorjai, *J. Am. Chem. Soc.*, 2016, **138**, 726–729.
- 16 M. Takeuchi, N. Matubayasi, Y. Kameda, B. Minofar, S.-i. Ishiguro and Y. Umebayashi, *J. Phys. Chem. B*, 2012, **116**, 6476–6487.
- 17 M. Nie, D. P. Abraham, D. M. Seo, Y. Chen, A. Bose and B. L. Lucht, *J. Phys. Chem. C*, 2013, **117**, 25381–25389.
- 18 D. M. Seo, S. Reininger, M. Kutcher, K. Redmond, W. B. Euler and B. L. Lucht, *J. Phys. Chem. C*, 2015, **119**, 14038–14046.
- 19 J. L. Allen, O. Borodin, D. M. Seo and W. A. Henderson, *J. Power Sources*, 2014, **267**, 821–830.
- 20 Y. Horowitz, H.-G. Steinrück, H.-L. Han, C. Cao, I. I. Abate, Y. Tsao, M. F. Toney and G. A. Somorjai, *Nano Lett.*, 2018, **18**, 2105–2111.
- 21 Y. Horowitz, H.-L. Han, F. A. Soto, W. T. Ralston, P. B. Balbuena and G. A. Somorjai, *Nano Lett.*, 2018, **18**, 1145–1151.
- 22 O. Borodin, M. Olguin, P. Ganesh, P. R. C. Kent, J. L. Allen and W. A. Henderson, *Phys. Chem. Chem. Phys.*, 2016, **18**, 164–175.
- 23 J. E. Katon and M. D. Cohen, *Can. J. Chem.*, 1975, **53**, 1378–1386.
- 24 I. Braschi, G. Gatti, C. Bisio, G. Berlier, V. Sacchetto, M. Cossi and L. Marchese, *J. Phys. Chem. C*, 2012, **116**, 6943–6952.
- 25 C. L. Angell, *Trans. Faraday Soc.*, 1956, **52**, 1178–1183.
- 26 Y. Ikezawa and H. Nishi, *Electrochim. Acta*, 2008, **53**, 3663–3669.
- 27 R. Aroca, M. Nazri, G. A. Nazri, A. J. Camargo and M. Trsic, *J. Solution Chem.*, 2000, **29**, 1047–1060.
- 28 H. G. Mayfield and W. E. Bull, *J. Chem. Soc. A*, 1971, 2279–2281.
- 29 G. M. Veith, B. L. Armstrong, H. Wang, S. Karnaas, W. E. Tenhaeff and M. L. Patterson, *ACS Energy Lett.*, 2017, 2084–2088.
- 30 K. A. Hays, B. Key, J. Li, D. L. Wood and G. M. Veith, *J. Phys. Chem. C*, 2018, **122**, 9746–9754.
- 31 L. J. Bellamy, *The Infra-red Spectra of Complex Molecules*, Chapman and Hall, London, 1975.
- 32 N. J. Kramer, K. S. Schramke and U. R. Kortshagen, *Nano Lett.*, 2015, **15**, 5597–5603.
- 33 M. P. Hanrahan, E. L. Fought, T. L. Windus, L. M. Wheeler, N. C. Anderson, N. R. Neale and A. J. Rossini, *Chem. Mater.*, 2017, **29**, 10339–10351.
- 34 G. M. Veith, L. Baggetto, R. L. Sacci, R. R. Unocic, W. E. Tenhaeff and J. F. Browning, *Chem. Commun.*, 2014, **50**, 3081–3084.
- 35 J. Coyle, C. Apblett, M. Brumbach, J. Ohlhausen and C. Stoldt, *J. Vac. Sci. Technol., A*, 2017, **35**, 061509.

- 36 J. Coyle, C. A. Appleby, G. M. Veith and C. R. Stoldt, *Meeting Abstracts*, 2018, MA2018–vol. 1, p. 38.
- 37 M. H. Brooker and J. B. Bates, *J. Chem. Phys.*, 1971, **54**, 4788–4796.
- 38 U. R. Kortshagen, R. M. Sankaran, R. N. Pereira, S. L. Girshick, J. J. Wu and E. S. Aydil, *Chem. Rev.*, 2016, **116**, 11061–11127.
- 39 L. M. Wheeler, N. C. Anderson, P. K. B. Palomaki, J. L. Blackburn, J. C. Johnson and N. R. Neale, *Chem. Mater.*, 2015, **27**, 6869–6878.
- 40 M. P. Hanrahan, Y. Chen, R. Blome-Fernández, J. L. Stein, G. F. Pach, M. A. S. Adamson, N. R. Neale, B. M. Cossairt, J. Vela and A. J. Rossini, *J. Am. Chem. Soc.*, 2019, **141**, 15532–15546.
- 41 G. M. Carroll, R. Limpens and N. R. Neale, *Nano Lett.*, 2018, **18**, 3118–3124.
- 42 S. Jiang, B. Hu, R. Sahore, H. Liu, G. F. Pach, G. M. Carroll, L. Zhang, B. Zhao, N. R. Neale and Z. Zhang, *ACS Appl. Energy Mater.*, 2019, **2**, 6176–6183.
- 43 M. H. Brodsky, M. Cardona and J. J. Cuomo, *Phys. Rev. B: Solid State*, 1977, **16**, 3556–3571.
- 44 U. S. Vogl, P. K. Das, A. Z. Weber, M. Winter, R. Kostecki and S. F. Lux, *Langmuir*, 2014, **30**, 10299–10307.
- 45 L. M. Wheeler, N. R. Neale, T. Chen and U. R. Kortshagen, *Nat. Commun.*, 2013, **4**, 2197.
- 46 A. Jarry, S. Gottis, Y.-S. Yu, J. Roque-Rosell, C. Kim, J. Cabana, J. Kerr and R. Kostecki, *J. Am. Chem. Soc.*, 2015, **137**, 3533–3539.